SI

Cascade-catalysed nanocarrier degradation for regulating metabolism homeostasis and enhancing drug penetration on breast cancer

Fang Zhang [a 1], Kai Cheng [a 1], Xiao-Shuai Zhang [b 1], Sui Zhou [a], Jia-Hua Zou [a, c], Ming-Yu Tian [a], Xiao-Lin Hou [a], Yong-Guo Hu [a], Jing Yuan [a], Jin-Xuan Fan [a*], Yuan-Di Zhao [a, d*], Tian-Cai Liu [e, f*]

[a] Britton Chance Center for Biomedical Photonics at Wuhan National Laboratory for Optoelectronics - Hubei Bioinformatics & Molecular Imaging Key Laboratory, Department of Biomedical Engineering, College of Life Science and Technology, Huazhong University of Science and Technology, Wuhan 430074, Hubei, P. R. China.

[b] Basic Medical Laboratory, General Hospital of Central Theater Command, Wuhan 430081, Hubei, P. R. China.

[c] Department of Oncology, Huanggang Central Hospital of Yangtze University, Huanggang 438000, Hubei, P. R. China.

[d] NMPA Research Base of Regulatory Science for Medical Devices & Institute of Regulatory Science for Medical Devices, Huazhong University of Science and Technology, Wuhan 430074, Hubei, P. R. China.

[e] Key Laboratory of Antibody Engineering of Guangdong Higher Education Institutes, School of Laboratory Medicine and Biotechnology, Southern Medical University, Guangzhou 510515, Guangdong, P. R. China.

[f] Guangdong Provincial Key Laboratory of Construction and Detection in Tissue Engineering, Southern Medical University, Guangzhou 510515, Guangdong, P. R. China.

* Corresponding author
Tel: 86-27-87792235, Fax: 86-27-87792202
E-mail address: jxfan@hust.edu.cn (J.X. Fan); zydi@mail.hust.edu.cn (Y.D. Zhao); liutc@smu.edu.cn (T.C. Liu)

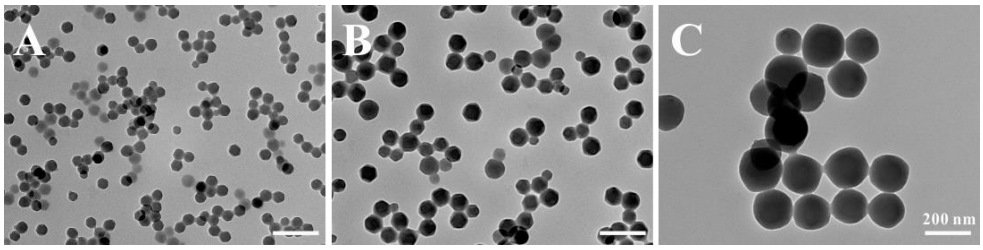

Figure S1. Effect of different ratio of Cu^{2+} and 2-MI doping ratios in Cu-ZIF-8 on the morphology, the doping ratio were 0.02 (A), 0.05 (B) and 0.2 (C), respectively.

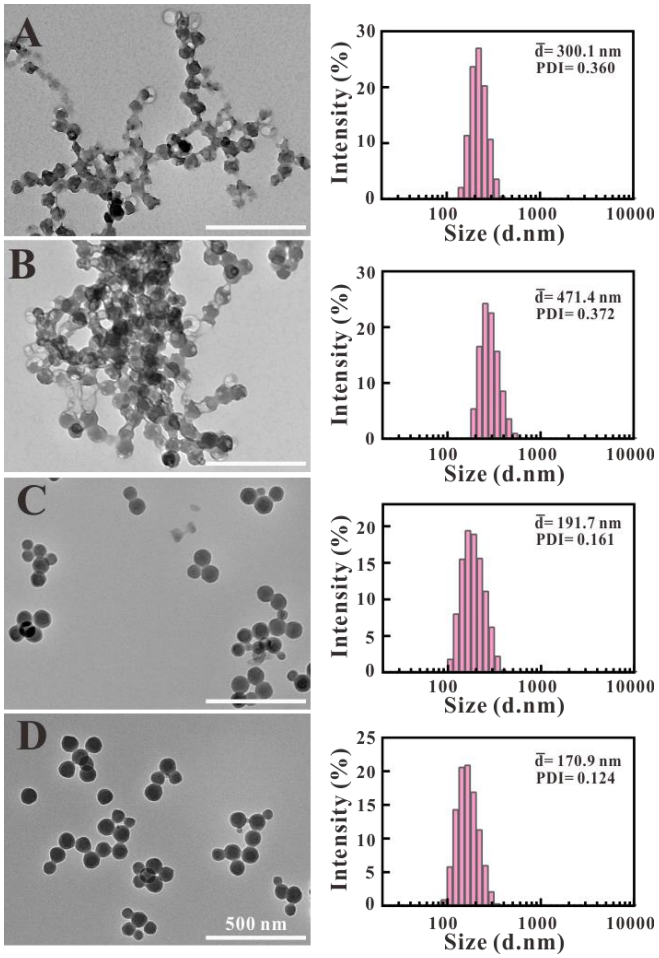

Figure S2. Effect of different ratio of Cu-ZIF-8 carrier to drug on the morphology and particle size distribution of GC@Cu-Z, 8:1 (A), 4:1 (B), 2:1 (C), 1:1 (D).

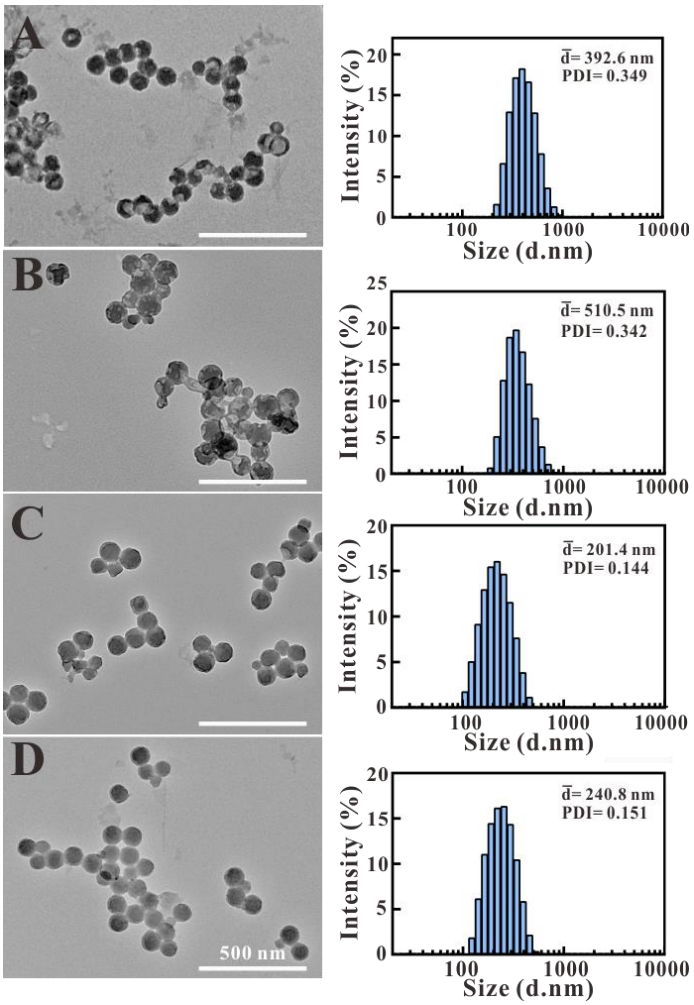

Figure S3. Effect of different ratio of Cu-ZIF-8 carrier to drug on the morphology and particle size distribution of GC@Cu-Z@HA, 8:1 (A), 4:1 (B), 2:1 (C), 1:1 (D).

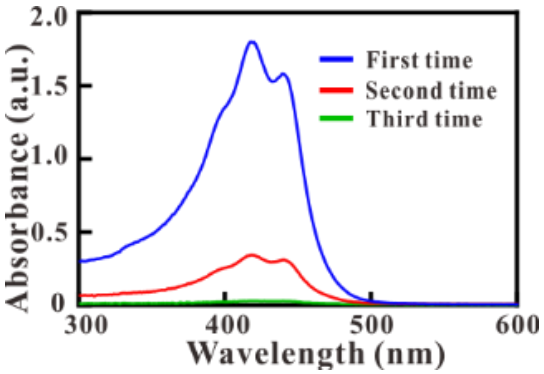

Figure S4. The UV-vis absorption spectra of the supernatant after centrifugation at different times.

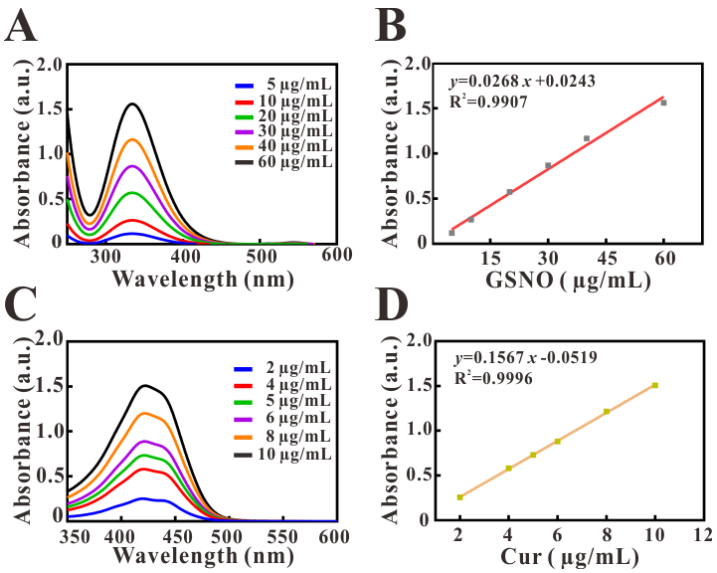

Figure S5. The standard curves of GSNO and Cur. The UV-vis absorption spectra of different concentration of GSNO (A) and Cur (C), and the corresponding standard absorption curve at the characteristic absorption peak of 340 nm (B) and 430 nm (D).

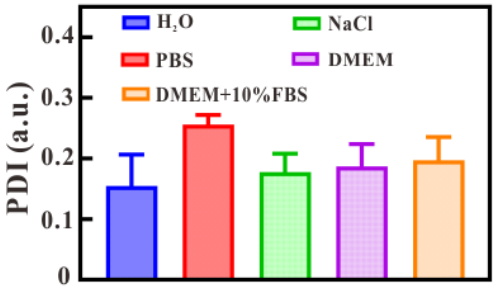

Figure S6. The polydispersity index PDI of GC@Cu-Z@HA nanocarrier in different solution.

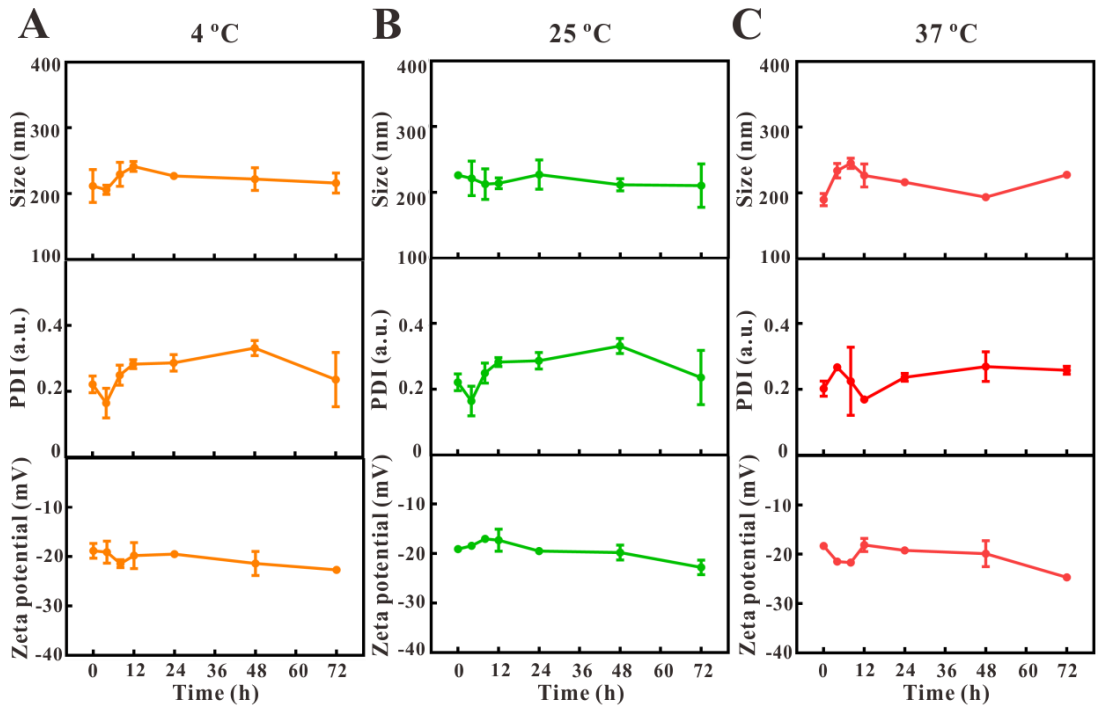

Figure S7. The stability study of nanocarrier. The change of hydrated particle size, Zeta potential and PDI of GC@Cu-Z@HA with time at 4 ºC (A), 25 ºC (B), and 37 ºC (C).

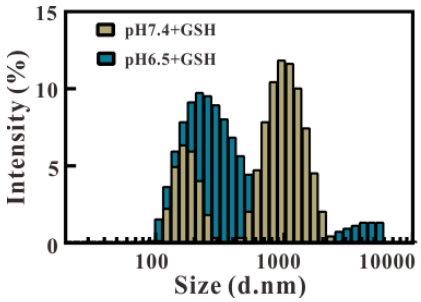

Figure S8. The hydrated particle size change of GC@Cu-Z@HA at different condition for 4 h storage.

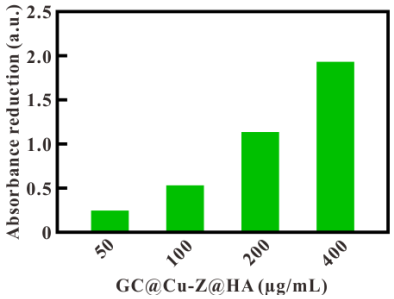

Figure S9. The effect of ·OH on MB absorption at 660 nm through Fenton-like reaction treated with different concentration of GC@Cu-Z@HA.

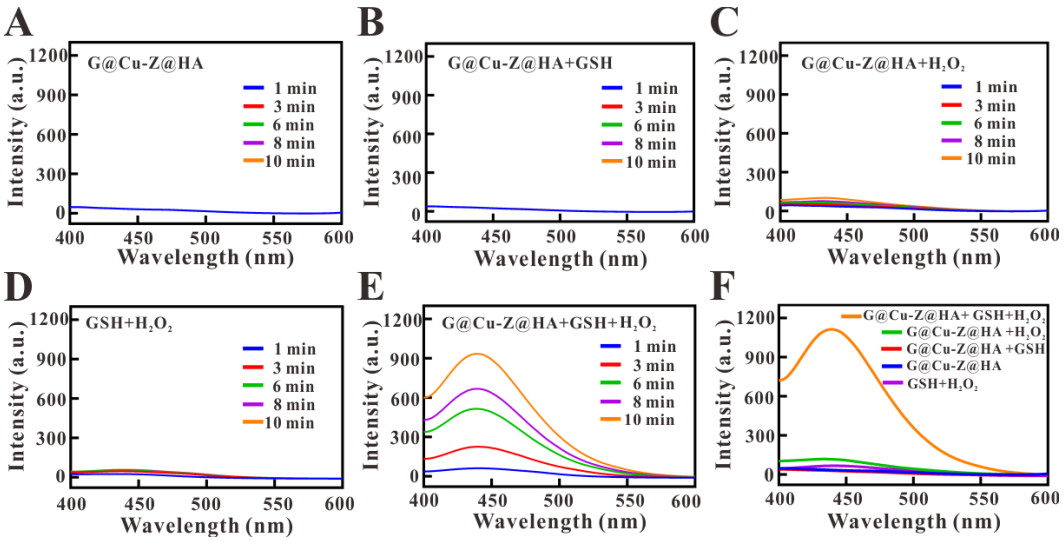

Figure S10. Fluorescence change of ·OH generation by G@Cu-Z@HA using TA under different treatments (A-E); and the comparative fluorescence plot after 10 min (F).

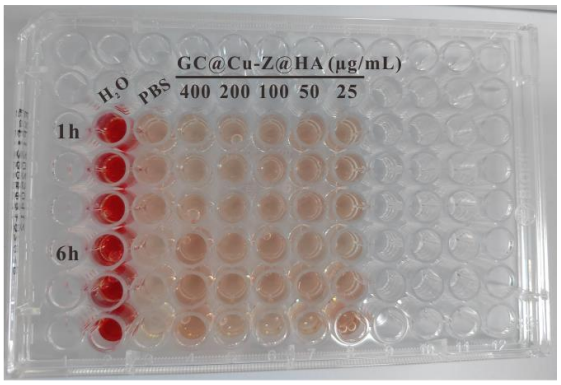

Figure S11. The supernatant of red blood cell incubated with different concentration of GC@Cu-Z@HA.

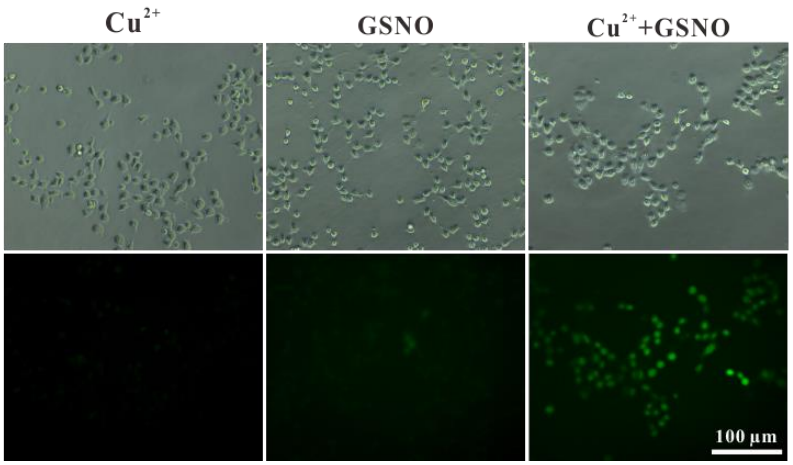

Figure S12. The fluorescence imaging of NO produced by 4T1 cell using DAF-FM DA under different treatments.

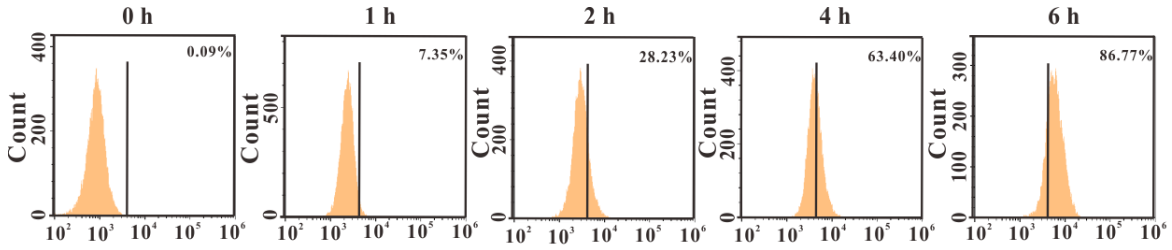

Figure S13. Quantificationally analyzed of Cur fluorescence intensity in 4T1 cell after GC@Cu-Z@HA incubation for different times by flow cytometer.

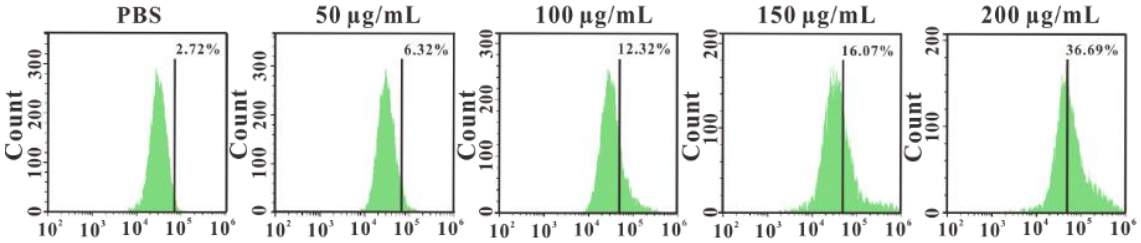

Figure S14. Flow cytometry of ROS in 4T1 cell with different treatments by DCFH-DA.

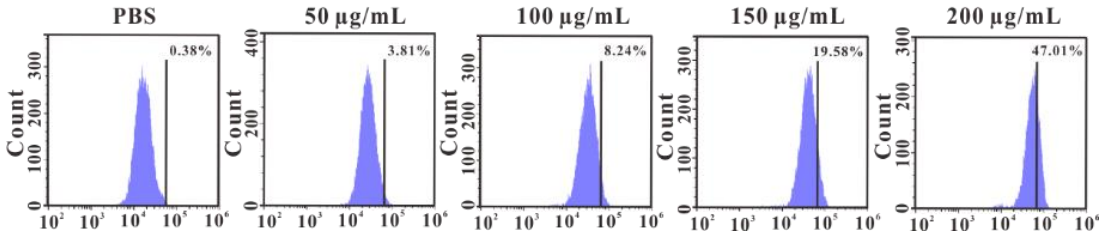

Figure S15. Flow cytometry of NO in 4T1 cell with different treatments by DAF-FM DA.

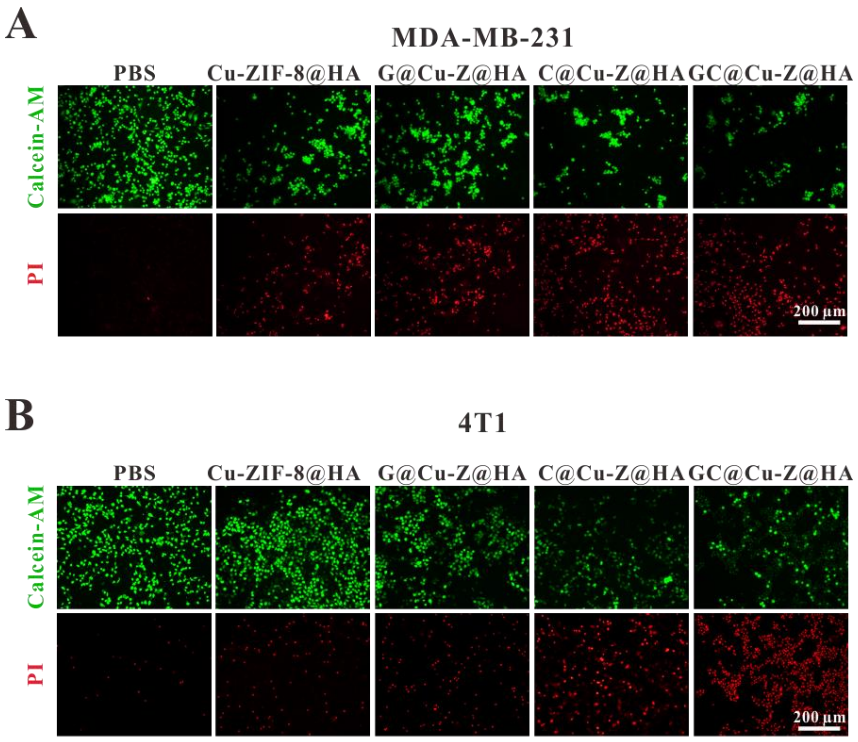

Figure S16. Fluorescence imaging of Calcein-AM and PI staining MDA-MB-231 (A) and 4T1 cells (B) with different treatments.

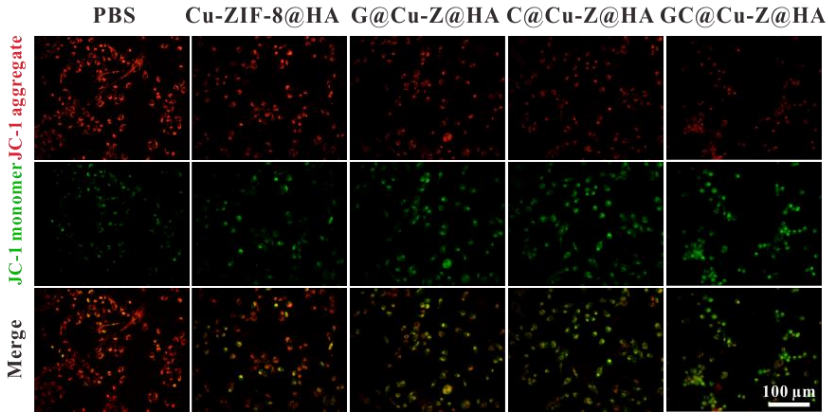

Figure S17. Fluorescence imaging of mitochondrial membrane potential detected by JC-1 dye in MDA-MB-231 cell after different treatments.

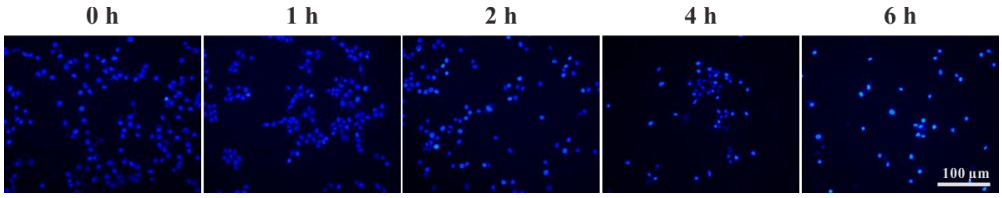

Figure S18. The apoptosis of 4T1 cell monitoring by Hoechst 33342 staining after treated with GC@Cu-Z@HA at different time points.

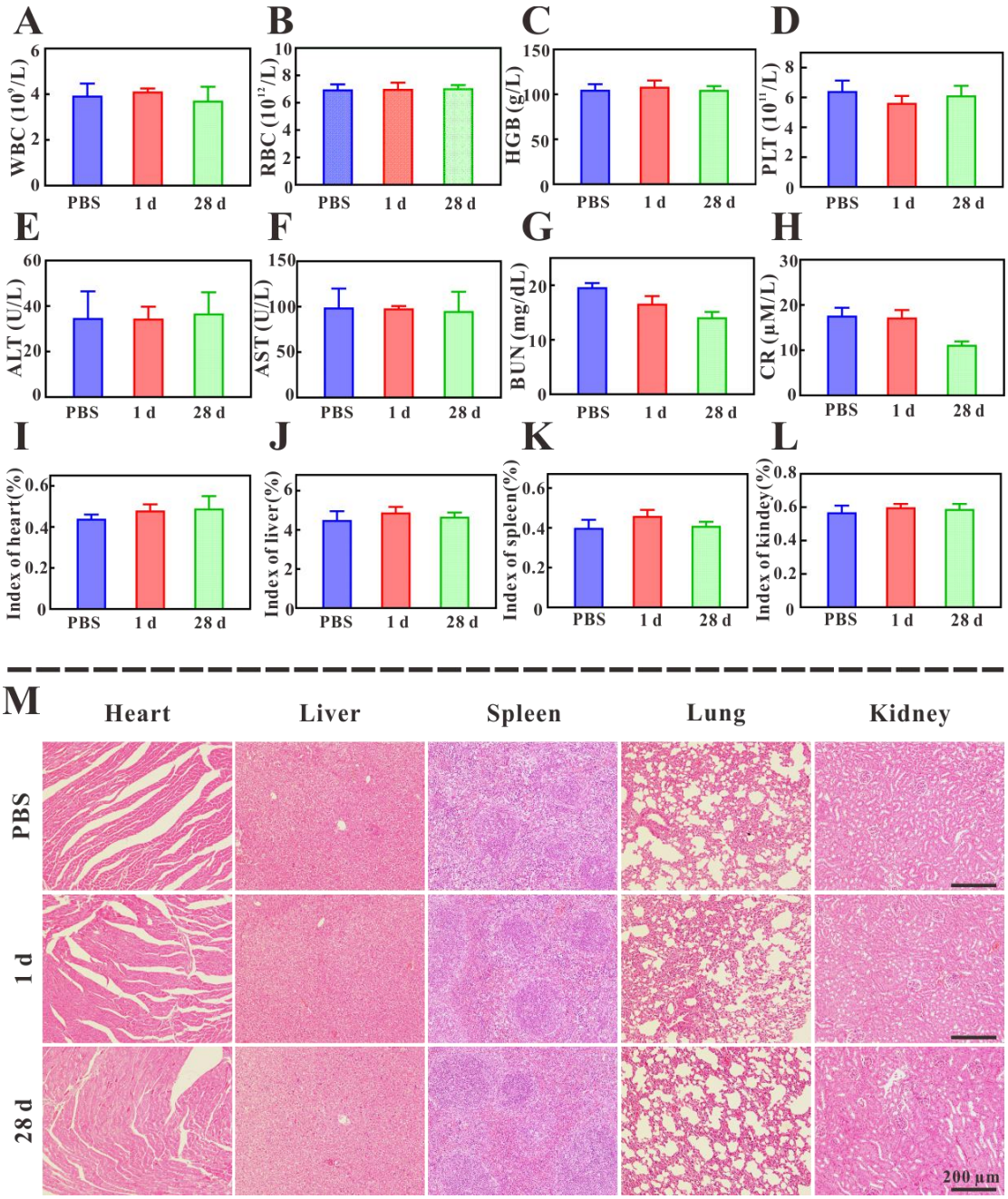

Figure S19. *In vivo* biosafety evaluation of nanocarrier. Blood analysis after single injection and multiple injections of GC@Cu-Z@HA in healthy mice: WBC (A), RBC (B), HGB (C), PLT (D), ALT (E), AST (F), BUN (G), CR (H); various organ indexes of heart, liver, spleen and kidney (I-L) and H&E staining of major organs (M); n = 5.

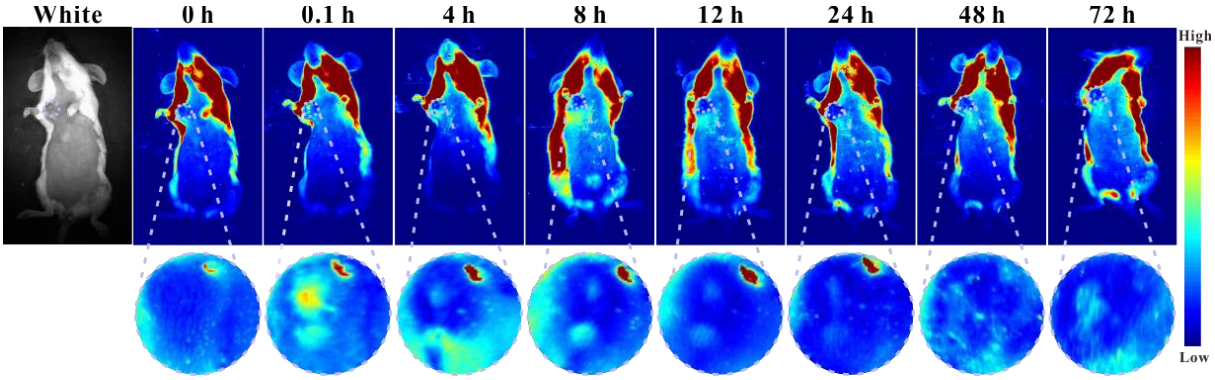

Figure S20. Fluorescence imaging and magnification of tumor site of 4T1 orthotopic bearing mice injected with GC@Cu-Z@HA by intratumoral injection at different time points.

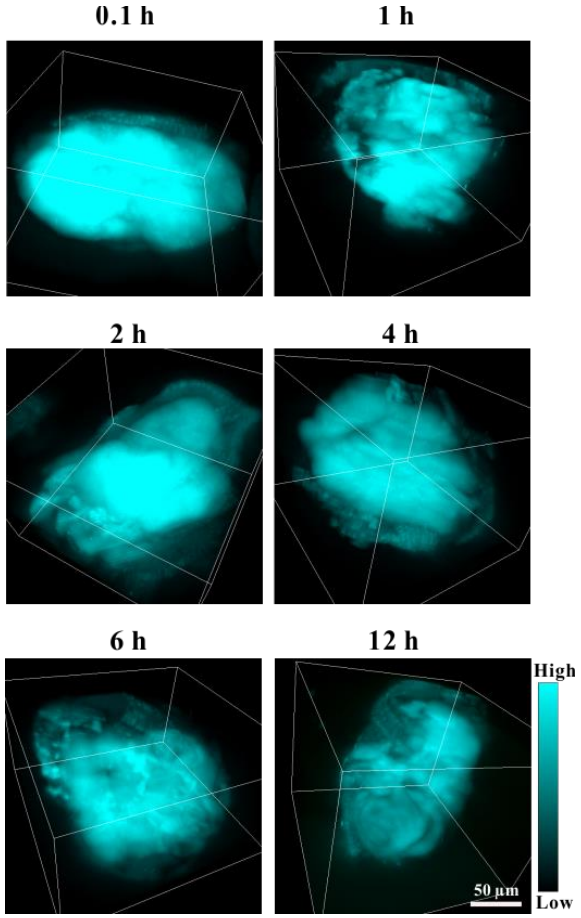

Figure S21. 3D deep-hypothermia fluorescence imaging of NADPH of orthotopic breast cancer mice at different times after injection of G@Cu-Z@HA.

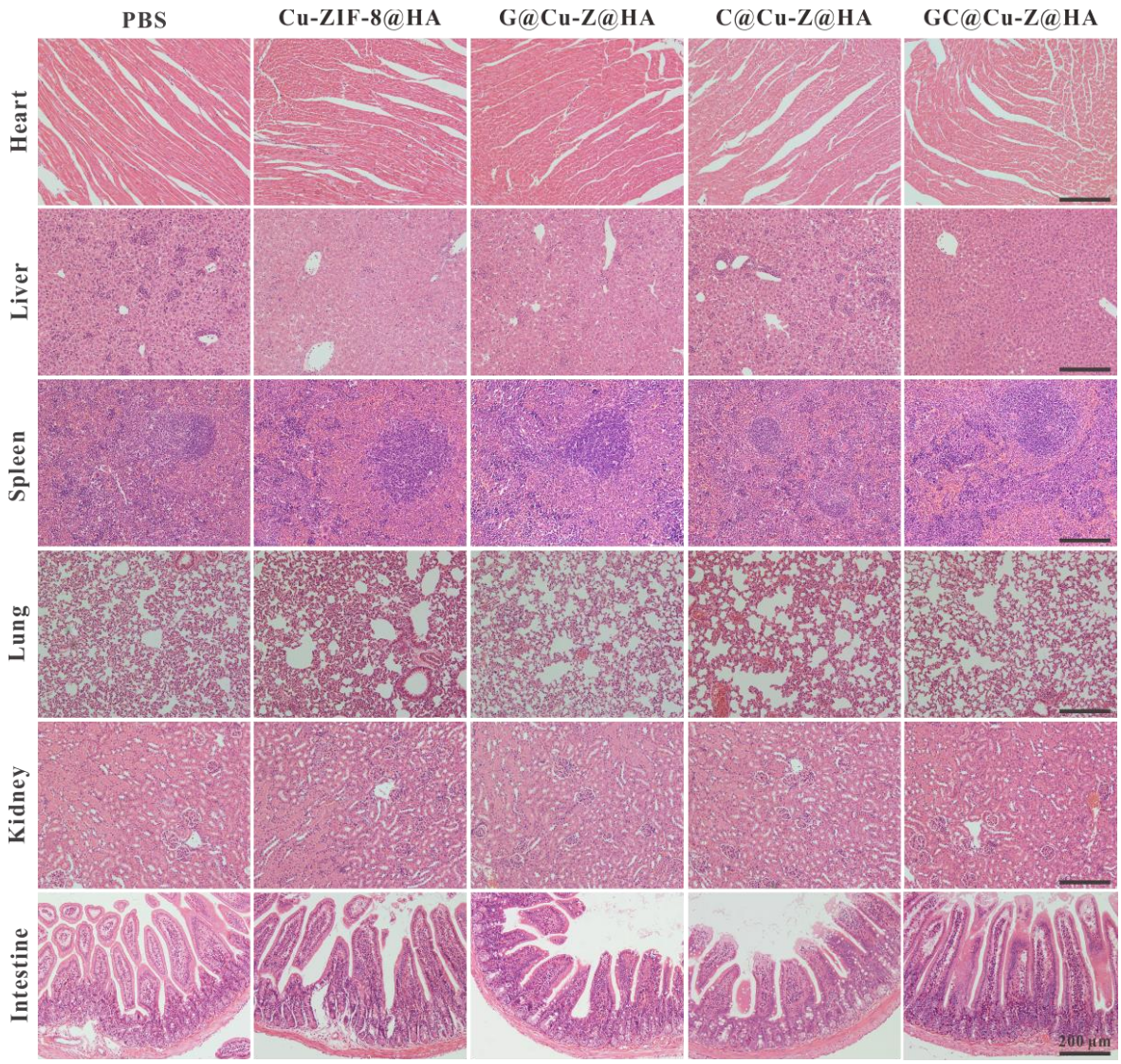

Figure S22. H&E staining of heart, liver, spleen, lung, kidney and intestine of 4T1 orthotopic bearing mice after different treatments.

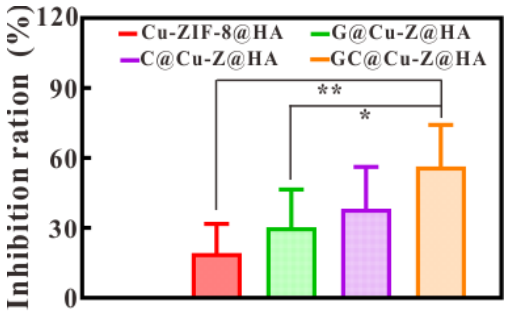

Figure S23. Tumor inhibition rate of 4T1 orthotopic bearing mice after different treatments; n=5, *: p <0.05, **: p <0.01.

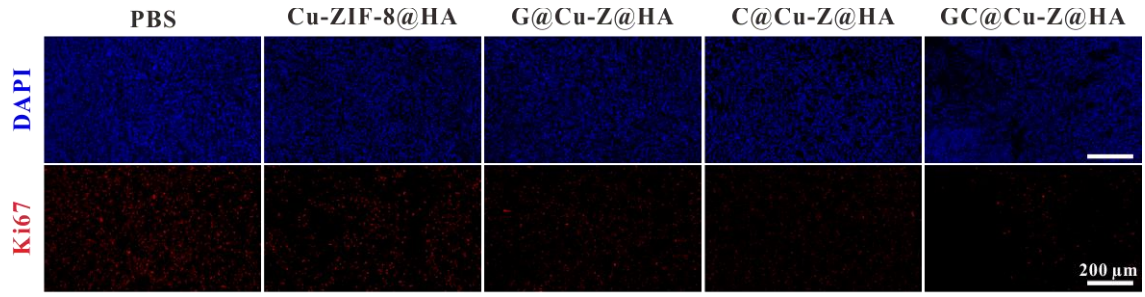

Figure S24. Ki67 immunofluorescence imaging of tumor tissue in 4T1 orthotopic bearing mice after different treatments.

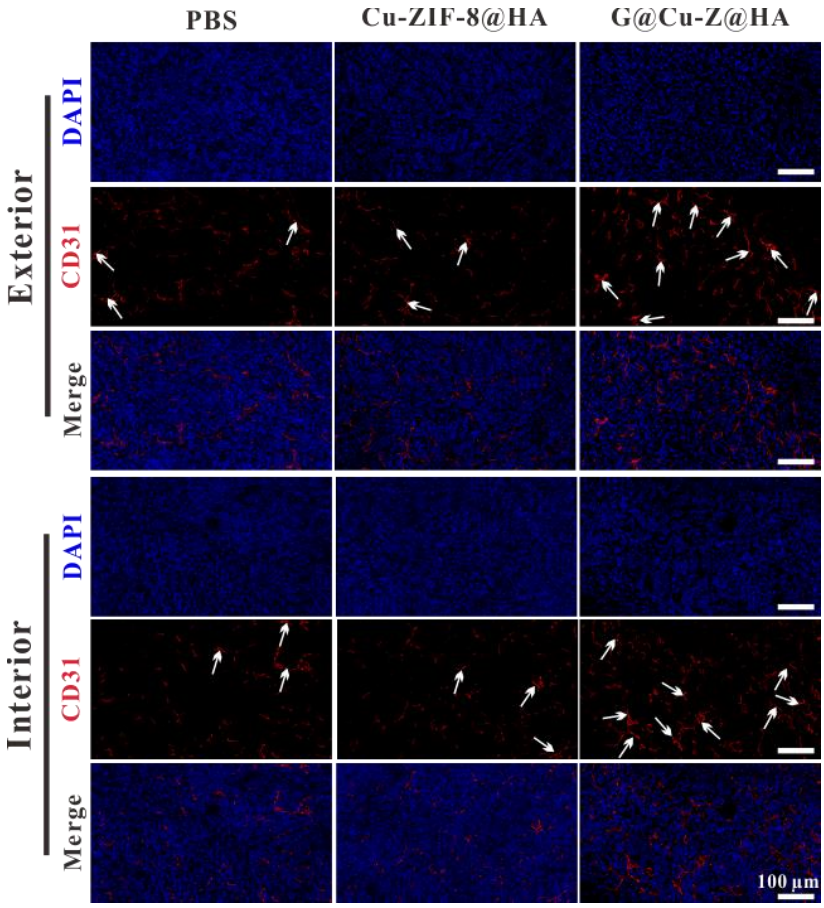

Figure S25. Immunofluorescence imaging of tumor blood vessel in the exterior and interior layer of tumor slice stained by anti-CD31 after different treatments.